University of Nebraska - Lincoln

Spring April 30, 2010

Numerical modelling of a 10-cm-long multi-GeV laser wakefield accelerator driven by a self-guided petawatt pulse

Serguei Y. Kalmykov
Sunghwan A. Yi
Arnaud Beck
Agustin F. Lifschitz
Xavier Davoine, et al.

Numerical modelling of a 10-cm-long multi-GeV laser wakefield accelerator driven by a self-guided petawatt pulse

Numerical modelling of a 10-cm-long multi-GeV laser wakefield accelerator driven by a self-guided petawatt pulse

S Y Kalmykov[1,5], **S A Yi**[1], **A Beck**[2], **A F Lifschitz**[3], **X Davoine**[2],
E Lefebvre[2], **A Pukhov**[4], **V Khudik**[1], **G Shvets**[1], **S A Reed**[1],
P Dong[1], **X Wang**[1], **D Du**[1], **S Bedacht**[1], **R Zgadzaj**[1],
W Henderson[1], **A Bernstein**[1], **G Dyer**[1], **M Martinez**[1], **E Gaul**[1],
T Ditmire[1] **and M C Downer**[1]

[1] Department of Physics, University of Texas at Austin, One University Station
C1500, Austin, TX 78712, USA
[2] CEA, DAM, DIF, Bruyères-le-Châtel, 91297 Arpajon Cedex, France
[3] Laboratoire de Physique des Gaz et des Plasmas, Université Paris XI/CNRS,
Bâtiment 210, 91405 Orsay Cedex, France
[4] Institut für Theoretische Physik I, Heinrich-Heine-Universität Düsseldorf,
40225 Düsseldorf, Germany
E-mail: kalmykov@physics.utexas.edu

Abstract. The use of a short-pulse petawatt (PW) laser ($\tau_L < 200\,\text{fs}$, wavelength $\approx 1\,\mu\text{m}$) enables experimental realization of a self-guided, multi-centimetre-long multi-GeV laser wakefield electron accelerator. A comprehensive set of numerical simulations showed that a 150 fs, 1.33 PW pulse is self-guided over 10 cm of a static filling gaseous plasma of density $1\text{--}3 \times 10^{17}\,\text{cm}^{-3}$ and is stable against relativistic filamentation. A fully broken electromagnetic wake (electron density 'bubble') is excited over the entire interaction length. Variations of bubble size and shape associated with nonlinear evolution of the driving pulse result in self-injection of background plasma electrons. Self-injection begins immediately after the first nonlinear laser focus, where pulse de-focusing forces the bubble to grow. Injection continues without interruption while the bubble expands, and ceases when the laser becomes self-guided and

[5] Author to whom any correspondence should be addressed.

IOP Institute of Physics Φ DEUTSCHE PHYSIKALISCHE GESELLSCHAFT

bubble evolution stabilizes. Self-injected electrons are accelerated to $\sim 7\,\text{GeV}$ with less than 10% energy spread and $\sim 1.3\,\text{nC}$ charge. Numerical modelling of the laser pulse dynamics over the entire plasma length is carried out using a time-averaged, fully relativistic, quasi-static three-dimensional (3D) axi-symmetric particle-in-cell (PIC) code, WAKE. The process of electron self-injection is explored by means of both test-particle modelling (WAKE) and 3D PIC simulations using the recently developed CALDER-Circ code in quasi-cylindrical geometry.

Contents

1. Introduction

The advent of ultrashort-pulse ($<150\,\text{fs}$) petawatt (PW) laser technology [1]–[5] opens a path towards implementation of high-energy laser wakefield electron accelerators (LWFA) [6, 7]. In the original, weakly nonlinear LWFA [8], the radiation pressure of a short laser pulse (shorter than the electron plasma oscillation period) excites a trailing plasma wave (laser wakefield) with a relativistic phase velocity. The wake, in turn, effectively traps externally injected electrons and accelerates them to GeV energy [6, 9, 10]. The stringent requirement of external injection can be bypassed if LWFA operates in the strongly nonlinear blowout regime [11]–[13]. In this regime, the plasma electrons are radially expelled by the ponderomotive force (while heavy ions remain immobile), and the wake becomes a cavity devoid of electrons trailing behind the driver. This structure readily self-injects electrons from ambient plasma [14], which is favourable for a single-stage generation of GeV-class quasi-monoenergetic electron bunches out of centimetre-long plasmas [15]–[20]. Further experimental progress towards higher quality and energy of electron bunches requires investment in laser power [7] and, hence, advanced amplification and compression techniques (such as optical parametric chirped-pulse amplification, OPCPA [5, 21]).

To benefit from the PW power and short pulse duration ($\tau_L \sim 100\,\text{fs}$), the GeV LWFA should meet certain requirements to ensure (i) laser pulse stability and (ii) excitation of

a strongly nonlinear wake over the entire laser–plasma interaction (LPI) length. A trade-off between the electron plasma density n_0, which prescribes the characteristic acceleration gradient [22]

$$E_{\text{acc}} \, (\text{V cm}^{-1}) \approx 0.96 n_0^{1/2} \, (\text{cm}^{-3}),$$

and plasma length (a few centimetres, as imposed by target design limitations) makes it at present desirable to work in the range $n_0 > 10^{17} \, \text{cm}^{-3}$. In this case, a PW laser with a wavelength $\lambda_0 \approx 1 \, \mu\text{m}$ is about an order of magnitude overcritical for the relativistic self-focusing (RSF) [23]. Threat of catastrophic self-focusing and transverse beam break-up due to filamentation [24] can be avoided only if the pulse is shorter than a plasma period, $\tau_L < 2\pi/\omega_{\text{pe}}$, where $\omega_{\text{pe}} = (4\pi e^2 n_0/m_e)^{1/2}$ is the plasma frequency, e is the electron charge and m_e is the electron rest mass. In practical units,

$$\tau_L(\text{fs}) < 10^{11} n_0^{-1/2} \, (\text{cm}^{-3}). \tag{1}$$

Once condition (1) holds, the LPI length is limited by either diffraction (for $\omega_{\text{pe}}\tau_L < 1$) [6, 25] or laser depletion due to the wake excitation (for $1 < \omega_{\text{pe}}\tau_L < 2\pi$) [7]. The latter regime is relevant to the self-guided LWFA with full electron blowout, which is the focus of the present paper. With the pulse duration restricted by condition (1), the depletion length [26], $L_{\text{depl}} \approx (\omega_0/\omega_{\text{pe}})^2 c\tau_L$, can be expressed as

$$L_{\text{depl}} \, (\text{cm}) < 3.4 \times 10^{27} \lambda_0^{-2} \, (\mu\text{m}) n_0^{-3/2} \, (\text{cm}^{-3}), \tag{2}$$

where $\lambda_0 = 2\pi c/\omega_0$ and ω_0 is the laser frequency. For a plasma density $n_0 = 2.5 \times 10^{17} \, \text{cm}^{-3}$ and laser wavelength $\lambda_0 = 1.057 \, \mu\text{m}$, $1 \, \text{PW} \approx 15 P_{\text{cr}}$; equations (1) and (2) give $\tau_L < 200 \, \text{fs}$ and $L_{\text{depl}} < 24.5 \, \text{cm}$, respectively. The expected electron energy gain is thus above $10 \, \text{GeV}$.

This estimate sets a parameter scale for the extremely challenging regime of the PW laser-driven plasma accelerator. These parameters surpass by an order of magnitude those of state-of-the-art experiments with self-guided multi-terawatt (TW) lasers [17]–[20], where GeV electrons from much shorter plasmas (<1 cm) of more than an order of magnitude higher density are sporadically observed. PW power and sub-200 fs duration allows planning an experiment on a much larger scale aiming at better stability and multi-GeV energy gain. A recently commissioned Texas Petawatt (TPW) facility [3, 27, 28] offers a unique opportunity to accomplish such an experiment in the near future. The short-pulse TPW beamline (average power $P \approx 1.33 \, \text{PW}$) uses OPCPA technology and delivers a 200 J pulse of 150 fs duration (full-width at half-maximum in intensity), the shortest of existing PW lasers. The central wavelength is $\lambda_0 = 1.057 \, \mu\text{m}$. A 1 Hz repetition rate laser, POLARIS, with similar parameters is at present under construction at Friedrich-Schiller-Universität (Jena, Germany) [4].

The present paper discusses possible practical designs of the plasma wakefield accelerator driven by a self-guided sub-200 fs PW laser pulse and addresses the following issues. In what parameter range does the laser pulse stably self-guide and accelerate electrons in the blowout regime? How sensitive is the guided stage to the focusing geometry and imperfections of a focal spot (i.e. non-Gaussian shape, presence of hot spots and phase distortions)? What is the impact of imperfect focusing on the quality of the electron beam? How can we control self-injection and improve the quality of the accelerated electron bunch by manipulating the laser nonlinear focusing? These and other questions are answered in a set of multi-dimensional particle-in-cell (PIC) simulations.

The paper is organized as follows. As a reference point for the numerical study, we select the driving laser pulse with the TPW parameters and outline a possible strategy of the laboratory experiment in section 2. Numerical modelling of laser self-guiding and stability is the subject of section 3. The envisioned setup assumes weak laser beam focusing (with spot size $r_0 > 80 \, \mu$m) and an LPI length of 10 cm, which makes a full PIC simulation prohibitively long even in a planar two-dimensional (2D) geometry. As a consequence, we use a hybrid approach. Using a cylindrically symmetric, time-averaged quasi-static fully relativistic code, WAKE [29], we find that the 150 fs, PW pulse stably self-guides over 10 cm in the density range 1–$3 \times 10^{17} \, \text{cm}^{-3}$. Underlying approximations greatly speed up the WAKE simulation, but presume axial symmetry and exclude electron self-injection. To account for possible symmetry violation and electron trapping, the laser and wake stability in the presence of hot spots are studied using a fully explicit relativistic electromagnetic PIC code Virtual Laser Plasma Lab (VLPL) [30], in the planar 2D mode. The PW pulse shows remarkable stability against relativistic filamentation [24] in the density range 1–$3 \times 10^{17} \, \text{cm}^{-3}$. However, a few per cent energy spread of accelerated electrons is possible only if the focused laser beam is free of pronounced hot spots. Section 4 reports the study of electron self-injection in the blowout regime, which is done by means of both test-particle modelling (WAKE) and CALDER-Circ, a recently developed quasi-cylindrical 3D PIC code with Fourier decomposition of electromagnetic fields in the poloidal direction [31]. Laser spot size oscillations during the self-guiding in uniform plasmas cause periodic variations of the bubble size and periodic self-injection of ambient plasma electrons (as discussed in [32]). Bubble stabilization and contraction extinguishes the injection and effectively shortens electron bunch, simultaneously reducing its energy spread [14]. At low densities, $n_0 \sim 10^{17} \, \text{cm}^{-3}$, strong laser focusing, electron blowout and self-injection can be enforced by using a dense plasma slab as a short-focal-length thin plasma lens [33]. We find that electron self-injection in the density range 1–$3 \times 10^{17} \, \text{cm}^{-3}$ leads to quasi-monoenergetic electron acceleration to 2.5–7 GeV over 10 cm (with the final energy spread of 2–10%). The CALDER-Circ modelling predicts the following: bunch charge $\sim$1.3 nC, current 13.5–30 kA, and normalized transverse emittance 5–12π mm mrad. The main features of the nonlinear dynamics of the laser pulse, wakefield and accelerated electron bunch are summarized in section 5. The appendix describes numerical aspects of the quasi-cylindrical 3D PIC simulations.

2. Envisioned layout of LWFA experiment using the Texas Petawatt laser

A specific choice of the driving laser dictates the particular experimental configuration. Its detailed study, being important on its own, can also provide guidelines for planning experimental campaigns at similar facilities (e.g. POLARIS). The envisioned experiment sketched in figure 1 uses the benefits of the ultra-high power and intensity of the focused laser beam [27, 28]. Plasma channel and external electron injection are given up in favour of self-guiding and self-injection from ambient plasmas. Plasma is created by optical field ionization [34, 35] of a low-pressure helium gas backfill. The laser pulse is focused onto the millimetre-wide entrance port of a differentially pumped cell of adjustable length; radiation and accelerated electrons leave the cell through a few millimetre-wide exit aperture. The cell may have several compartments held at different pressures. The plasma may thus have a piecewise longitudinal density profile with relatively sharp transitions.
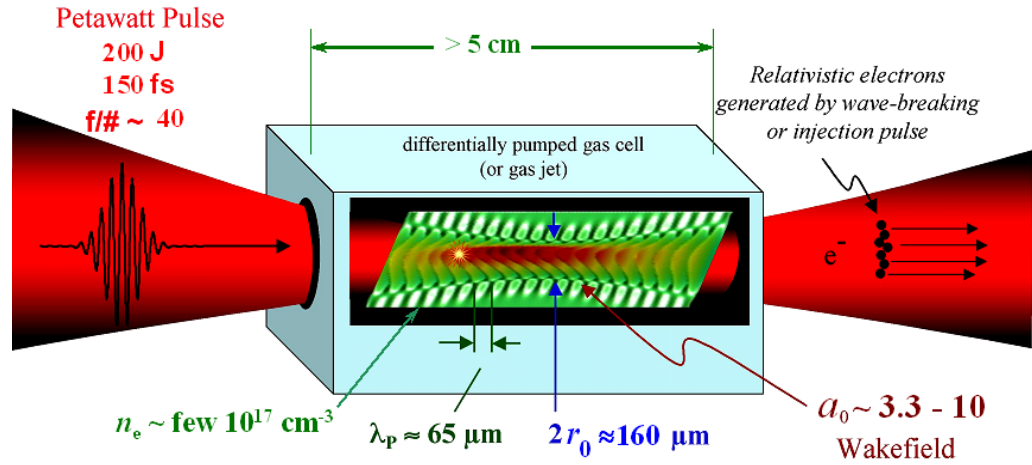
Figure 1. Sketch of the TPW LWFA experiment [28].

Numerical modelling shows that the range of densities 1–3×10^{17} cm^{-3} (corresponding to 2–6 Torr doubly ionized helium) is optimal from the standpoint of laser guiding, stability and electron self-injection. In this density range, the TPW laser is strongly overcritical, $8 < P/P_{cr} < 25$ (where $P_{cr} = 16.2\omega_0^2/\omega_{pe}^2$ GW is the critical power for the RSF [23]), and its normalized length belongs to the interval $2.7 < \omega_{pe}\tau_L < 4.2$. Hence, the pulse is long enough to avoid vacuum-like diffraction [6] (i.e. $\omega_{pe}\tau_L > 1$), and too short (i.e. shorter than a plasma period) to experience catastrophic RSF [29]. Such a pulse is expected to self-guide over 10 cm, which promises up to 6 GeV electron energy gain. Importantly, linear dephasing of the electron bunch, which occurs over the scale length $L_{deph} \approx 2\pi c\omega_0^2/\omega_{pe}^3 \approx 25$ cm, imposes no practical limitations.

The possible difficulty in tight focusing of the PW pulse (the actual spot size in the TPW experiment may be as large as 200 μm) can be used to the benefit of electron self-injection. As shown in section 3.2, a pulse initially mismatched for self-guiding goes through a few periods of strong focusing and de-focusing until the self-guiding sets in. As a result, the electron bubble experiences a relatively rapid variation in size and shape, which greatly facilitates electron self-injection [14]. In our case study, we shall mostly use the focal spot radius (at $\exp(-2)$ of the peak intensity) $r_0 = 80$ μm, which gives the focused peak intensity $I_{peak} = 1.35 \times 10^{19}$ W cm^{-2}. Simulations show that the wakefield remains quasi-static throughout the entire LPI length. This is favourable for visualization by frequency-domain holography [36, 37] with green probe and reference pulses split from the main pulse upstream of the amplifier chain.

3. Numerical modelling of laser dynamics

3.1. Layout and strategy of numerical experiments

Once the laser energy (200 J), duration ($\tau_L = 150$ fs) and spot size ($r_0 = 80$ μm) are chosen (in fact, in the experiment, they are prescribed by the amplifier and focusing system), electron density remains the only adjustable parameter. It turns out that this limited freedom makes it possible not only to achieve electron self-injection but also to vary the electron energy in a wide range while preserving beam quality (e.g. nC total charge and a few per cent energy spread).

Moreover, further optimization of self-injection is possible with the manipulation of electron density profiles.

Unless specified differently, all simulations below begin with the pulse Gaussian in space and time with the parameters specified in the previous paragraph. The pulse is focused on the plasma border $z = 0$ and propagates towards positive z. Preformed helium plasma spans from $z = 0$ to 10 cm and has a flat top profile (unless specified differently) with linear 1-mm-long density ramps at the entrance and exit. We build the simulation strategy upon the hybrid approach:

1. Laser self-guiding over the entire LPI distance is visualized in the quasi-static WAKE modelling.
2. Electron self-injection in the quasi-static wake is modelled with a test particle tracking code incorporated in WAKE.
3. Laser parameters from the regions where self-injection of test electrons is observed (e.g. vicinity of nonlinear foci) are extracted from the WAKE runs and used as an input for the non-quasi-static PIC runs.
4. Self-consistent dynamics of electron self-injection (initiation, termination and beam loading) is studied in the non-quasi-static quasi-cylindrical CALDER-Circ 3D PIC simulations [31].

3.2. Self-guiding of the PW pulse

The pulse self-guiding is modelled by the code WAKE in the extended paraxial approximation, which allows accurate calculation of the pulse group velocity and radiation absorption due to the creation of a plasma wake. The code is applicable when the beam spot size is well above λ_0 and the pulse duration is many laser cycles.

The first set of WAKE runs shows that as soon as the laser power and electron density are fixed, average parameters of the self-guided stage are quite insensitive to the initial spot size. This is favourable for the experiment because it allows for a considerable flexibility in focusing geometry: the focal spot can vary from $r_0 = 80\,\mu$m by a factor of 3 to either side. Simulations show that the average spot size and amplitude of the self-guided pulse are matched as $k_p r_{sg} \approx (3/2) a_{sg}^{1/2}$, where $k_p = \omega_{pe}/c$, $a = 0.85 I_{18}^{1/2} \lambda_0 (\mu$m$)$ is the normalized vector potential and I_{18} is the laser intensity in units of 10^{18} W cm^{-2}. Knowing that $P/P_{cr} = a_{sg}^2 (k_p r_{sg})^2/32$ [23], we find $a_{sg} \approx 2.4 (P/P_{cr})^{1/3}$ and $k_p r_{sg} \approx 2.3 (P/P_{cr})^{1/6}$. Parameters of the guided stage are thus prescribed by the ratio of the power to the critical power and are invariant with respect to the initial spot size/intensity of the beam.

Figure 2(a) displays the evolution of laser peak intensity for a plasma density $n_0 = 2.5 \times 10^{17}$ cm^{-3} (corresponding to $P/P_{cr} = 20$ and $\omega_{pe} \tau_L = 4.2$) and four different focal spot sizes (ranging from $r_0 = 27.4$ to $200\,\mu$m). The RSF, plasma wave-induced refraction and linear diffraction come to balance, and the self-guided stage begins before $z \approx 3$ cm (less than one-third of the entire LPI length) in all four runs. Formulae of the previous paragraph give $a_{sg} \approx 6.6$ and $k_p r_{sg} \approx 3.9$. Hence, the guided peak intensity and spot size are $I_{sg} \approx 5.4 \times 10^{19}$ W cm^{-2} and $r_{sg} \approx 40\,\mu$m (which agrees with the laser intensity profiles shown in figures 2(c) and (d)). One should note that, once the ratio P/P_{cr} is high (as in this example), even the perfectly matched beam ($r_0 = r_{sg}$, black dashed line in figure 2) shows considerable oscillations of the spot size and intensity before the self-guiding sets in. These oscillations, however, rapidly decay, whereas for
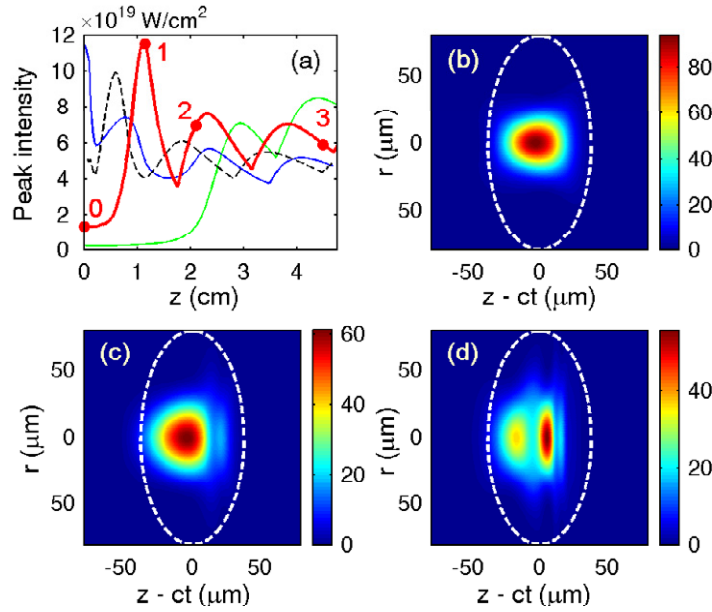
Figure 2. (a) Peak intensity of a 1.33 PW laser pulse for four initial spot sizes: $r_0 = 200\,\mu$m (green), $80\,\mu$m (red), $40\,\mu$m (dashed black) and $27.4\,\mu$m (blue). Plasma density is $n_0 = 2.5 \times 10^{17}\,$cm^{-3}. Self-guided stage with roughly the same average spot size and peak intensity is achieved in all four cases. Panels (b)–(d) depict the normalized intensity $|a|^2$ for positions labelled 1, 2 and 3, respectively, in panel (a). Broken iso-contour indicates intensity (at $\exp(-2)$ of the peak) in the beginning of simulation (position 0 in panel (a)); $z = ct$ is the trajectory of the pulse centre in vacuum.

a strongly mismatched beam ($r_0 > 2r_{sg}$) they remain on the 30% level over a few periods (red and green lines in figure 2(a)). We will show in section 4.2 that these oscillations result in periodic electron self-injection (see also [32]) and possible degradation of the electron energy spectrum.

The effect of plasma density on pulse propagation is displayed in figure 3, which shows (a) the variation of intensity, (b) energy losses and (c) frequency spectra of transmitted radiation for $n_0 = 5, 2.5$ and $1 \times 10^{17}\,$cm^{-3} ($P/P_{cr} = 40, 20$ and 8). In the first case, the pulse length is close to the plasma period, $\omega_{pe}\tau_L \approx 6$. Because of strongly uncompensated RSF, the pulse nearly collapses after the first 7.5 mm of propagation and clearly shows signatures of filamentation. As a result, the spot and intensity of the self-guided pulse rapidly oscillate. These features are typical of the dynamics of a too tightly focused overcritical pulse and are unfavourable for monoenergetic electron acceleration [38]. Self-guiding terminates around $z = 6\,$cm because of strong energy depletion ($>75\%$) and longitudinal beam break-up.

When $n_0 = 2.5 \times 10^{17}\,$cm^{-3} and $\omega_{pe}\tau_L \approx 4.2$ (red curve in figure 2(a) extended to $z = 10\,$cm), the pulse shows no tendency to collapse, although a strong initial focusing (by a factor 8.5 in intensity) is still the case. Self-guiding with a slowly varying spot size and peak intensity begins around $z \approx 1.5\,$cm. Laser energy depletion is 43% over 10 cm, which is consistent with the estimates presented in the introduction. Temporal compression of the pulse displayed in figure 2(d) contributes to guiding [39] after $\sim$3 cm of propagation. This is not the result of
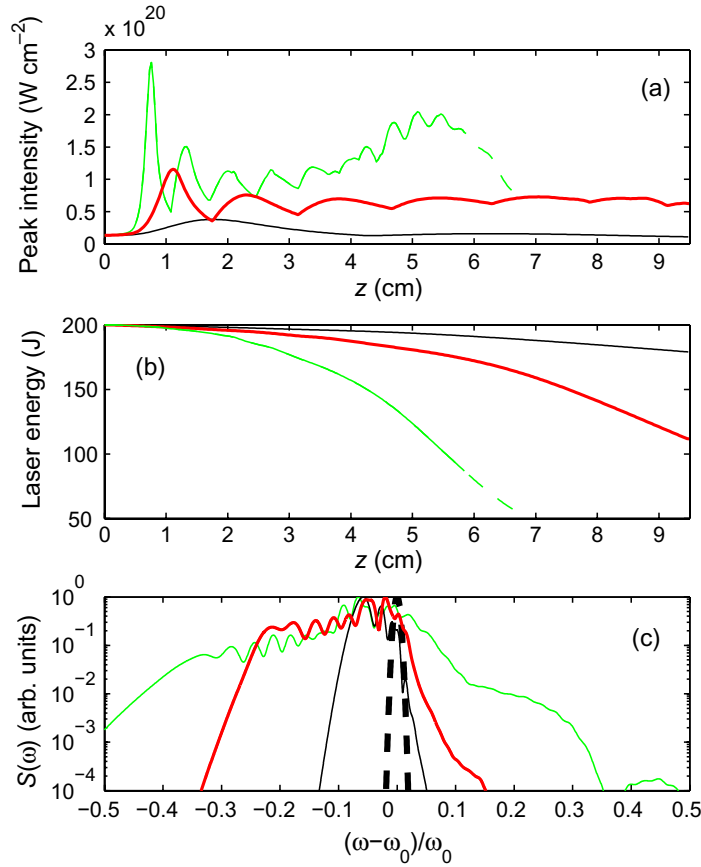
Figure 3. Self-guiding of the laser with $P = 1.33$ PW, $\tau_L = 150$ fs and initial spot size $r_0 = 80 \, \mu$m. Black: $n_0 = 10^{17}$ cm^{-3}; red: 2.5×10^{17} cm^{-3}; green: 5×10^{17} cm^{-3}. Panel (a) peak intensity versus propagation distance z; (b) laser energy versus z; (c) laser frequency spectrum (green—after propagation over 6 cm), thick dashed line—initial spectrum. Strong temporal compression of the pulse in plasma with $n_0 = 5 \times 10^{17}$ cm^{-3} (see the resulting spectral broadening in plot (c)) leads to the breakdown of the quasi-paraxial time-averaged simulation around $z = 6$ cm.

energy depletion (which is still below 10%) and can be explained as follows. In the self-guided regime, the rear part of the pulse is confined within an almost evacuated first wake bucket, whereas the pulse front witnesses the longitudinal gradient of the nonlinear refractive index at all times. The resulting frequency chirp broadens the laser spectrum, and the group velocity dispersion concurrently compresses the pulse. The spectral broadening to the red side (by $\sim -\omega_0/4$, according to figure 3(c)) can serve as an experimental diagnostic [40, 41].

When $n_0 = 10^{17}$ cm^{-3} ($\omega_{pe}\tau_L = 2.7$), the relativistic mass effect (which causes the RSF) partly compensates the electron density perturbation in the nonlinear refractive index [6]. Pulse intensity variations are minimal, and the depletion is negligible. Although the pulse is almost resonant for the excitation of the one-dimensional plasma wake [22], the transverse ponderomotive force is too weak (due to the large spot) to produce full blowout. Electron self-injection in this case can be achieved only if laser focusing is enforced artificially, as discussed in section 4.2.
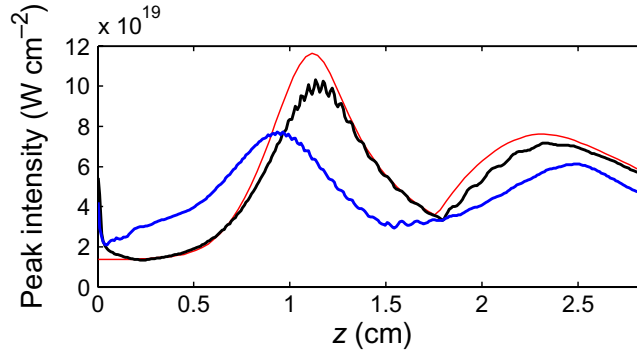
Figure 4. Effect of focal spot imperfections (hot spot and phase perturbation) on the PW pulse evolution in the plasma of density $n_0 = 2.5 \times 10^{17}\,\mathrm{cm}^{-3}$. Red line, a Gaussian pulse with an initially flat phase front (the same as red curves in figures 2(a) and 3(a)). Blue line, Gaussian pulse with a narrow super-Gaussian central spot and phase bump. Black line the same as the blue line, but without initial phase perturbation ($\varphi \equiv 0$). In all three cases, no transverse beam break-up occurs, and the laser pulse is self-guided after $z \approx 1.5\,\mathrm{cm}$.

3.3. Relativistic filamentation

Self-guiding of an initially Gaussian pulse appears to be very robust. A perfectly Gaussian focal spot, however, is unlikely to be achieved in the laboratory. The stability of a super-Gaussian pulse was established elsewhere [27]. Here, we study sensitivity of self-guiding and electron beam quality to the presence of intensity ('hot spots') and phase front perturbations in both quasi-static cylindrical (WAKE) and full 2D planar (VLPL) simulations. First, we consider cylindrical filamentation. The envelope of the normalized laser vector potential

$$a(r, z = 0, t) = \left(a_0\, \mathrm{e}^{-r^2/r_0^2 + \mathrm{i}\varphi(r)} + a_1\, \mathrm{e}^{-(r^2/r_1^2)^\alpha} \right) \mathrm{e}^{-2\ln 2\, t^2/\tau_L^2} \tag{3}$$

is taken as a boundary condition for the WAKE simulation. Here, $r = (x^2 + y^2)^{1/2}$, $r_1 \ll r_0$ and $\varphi = (\pi/3)[1 + r^2/(2r_1)^2]^{-1}$. Gaussian pulse simulations of figure 3 correspond to (3) with $a_1 = 0$ and $\varphi \equiv 0$. In addition to the super-Gaussian (of order α) hot spot, perturbation φ of the otherwise planar phase front represents another possible beam imperfection. The phase bump is large ($\varphi_{\max} = \pi/3$) and strongly localized. We present here the simulation for $\alpha = 4$, $a_0 = a_1 = 3.3$, $r_1 = 0.08 r_0 = 6.4\,\mu\mathrm{m}$ and $n_0 = 2.5 \times 10^{17}\,\mathrm{cm}^{-3}$. A super-Gaussian hot spot with such a small radius, $r_1 \approx 0.1\lambda_\mathrm{p}$ (where $\lambda_\mathrm{p} = 2\pi c/\omega_\mathrm{pe}$), is the most effective seed for pulse filamentation [24].

Diffraction of the hot spot and inhomogeneous focusing of the laser with a non-planar phase front produce transverse non-uniformity of the ponderomotive force (which, in turn, brings about radial modulation of the plasma density). The simulation of figure 4 shows that feedback from relativistic and ponderomotive nonlinearities is not strong enough to cause transverse beam break-up. A transient stage characterized by the formation of ring filaments takes less than 2 mm. The transients evolve towards long wavelengths and, finally, diffract out, leaving the guided beam almost intact, in full agreement with the conclusions of Andreev *et al* [24]. However, the strongly perturbed plasma wake uncontrollably traps a large amount of non-monoenergetic electrons. The long-term effect of that is assessed in a full PIC VLPL
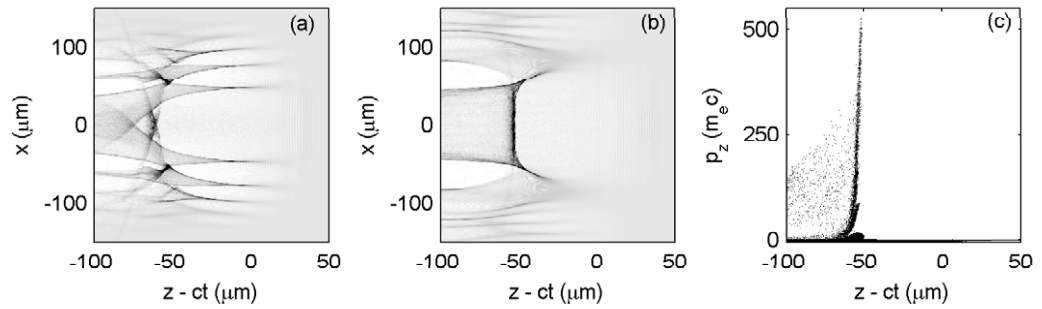
Figure 5. Effect of relativistic filamentation on the plasma wake in a planar geometry (planar 2D VLPL simulation). Laser radiation is polarized out of plane. Background density is $n_0 = 10^{17}\,\mathrm{cm}^{-3}$. The first two panels show electron density at (a) $z \approx 2.2\,\mathrm{mm}$ and (b) $z \approx 9.2\,\mathrm{mm}$. The greyscale is linear and spans from $n_0 = 0$ to $10^{18}\,\mathrm{cm}^{-3}$. Panel (c) shows the electron phase space at $z \approx 13.2\,\mathrm{mm}$. During the transient stage, the wake becomes sliced (panel (a)) and rapidly evolves. The resulting massive electron self-injection (evident in panels (b) and (c)) precludes quasi-monoenergetic acceleration.

simulation in planar geometry for a low density case, $n_0 = 10^{17}\,\mathrm{cm}^{-3}$. The initial condition is (3), where $r = x$, $\varphi \equiv 0$, $\alpha = 1$ (Gaussian hot spot), $a_1 = a_0/\sqrt{2} = 2.33$ and $r_1 = r_0/8 = 10\,\mu\mathrm{m}$. The laser is polarized out of plane. The first bucket of the plasma wave is shown in figure 5 for (a) $z \approx 2.2\,\mathrm{mm}$ (transient stage) and (b) $z = 9.2\,\mathrm{mm}$ (saturated stage). The development of non-quasi-static transient structures causes massive electron injection, and the wake bucket becomes overloaded. The bottom of the bucket, as seen in figures 5(b) and (c), is formed of a flat electron bunch with a continuous energy spectrum (no tendency for compression in the momentum/energy space was observed after propagation over 13.2 mm). Hence, because even a single hot spot can disrupt quasi-monoenergetic electron acceleration, a high-quality laser focus is mandatory.

4. Electron self-injection in the blowout regime

In this section, we review the basic features of the electron bubble as an accelerating structure, and emphasize the critical aspects for electron self-injection and acceleration. We rely on two different approaches that complement each other. In sections 4.1 and 4.2, we discuss electron self-injection in terms of a simple test-particle model. The model describes the evolution of initially quiescent test electrons in the electromagnetic fields of a self-consistently evolving quasi-static bubble (obtained in the WAKE simulation). A fully 3D test-particle tracking module built into the WAKE code is fully dynamic, relativistic and non-averaged in time. It accurately describes interaction of test electrons with both a quasi-paraxial high-frequency radiation beam (taking into account the linear laser polarization) and slowly varying quasi-static wakefields. For a given set of laser and plasma parameters, the observation of self-injection via test-particle modelling sufficiently motivates the subsequent time-consuming massively parallel 3D PIC simulations. It also localizes the regions along the laser path where self-injection is likely to occur (such as the vicinity of nonlinear laser foci) and thus assesses the amount of dark current. And, last but not least, it gives an upper estimate of electron energy and energy spread after 10 cm propagation.

The electron injection and acceleration during the period of bubble expansion and contraction (predicted in test-particle modelling) are reproduced in section 4.3 in fully dynamic mode, and with beam loading [42, 43] accounted for, in fully dynamic 3D PIC simulations. These simulations use the CALDER-Circ quasi-cylindrical code [31] and meaningfully predict the experimental outcome.

4.1. Qualitative physics of electron self-injection near a nonlinear laser focus

In this and the next subsection, we focus on the regime corresponding to the red curves in figures 2(a) and 3. We establish that self-injection of initially quiescent electrons occurs primarily because of the bubble evolution driven by nonlinear evolution of the laser.

An initially mismatched laser beam self-focuses to intensities above $10^{20}\,\mathrm{W\,cm^{-2}}$ and spot size $\sim 25\,\mu\mathrm{m}$. The intensity distribution in the focus can be seen in figure 2(b). Radiation pressure becomes so high as to expel all electrons facing the laser pulse. The expelled quasi-static macroparticles (black trajectories in figure 6(a)) are responsible for the formation of a bow wave [44]—the dense streak pointing in the radial direction in figure 6(c). Fully stripped heavy ions, however, remain at rest. The resulting field of charge separation attracts the bulk electrons (green trajectories in figure 6(a)) back to the axis. The bubble closes, and trajectories of the innermost electrons, as shown in figure 6(b), overshoot. The closed electron density cavity surrounded by a dense shell ('sheath') of relativistic electrons (red-coloured trajectories in figure 6(b)) trails behind the driving laser over the positive ion background. Figure 6(a) shows that electrons forming the sheath originate from the hollow cylinder with a shell thickness $\Delta r < k_\mathrm{p}^{-1}$ and radius close to the laser spot size. Figure 6(b) demonstrates that trajectories of the innermost sheath electrons pass through the regions of the highest slowly varying fields in the system (the peak accelerating and focusing fields exceed the cold wavebreaking limit, $E_\mathrm{br} \approx 0.5\,\mathrm{GV\,cm^{-1}}$, more than twice). Being exposed to these enormous forces, sheath electrons interact with the bubble the longest [14] (a detailed quasi-static description of their dynamics is presented in [45]). When approaching the point of trajectory crossing, they are already pre-accelerated, $\gamma_\mathrm{e} = (1 - v_\mathrm{e}^2/c^2)^{-1/2} \gg 1$ [46] and, hence, have a much higher inertia than the quasi-static electrons of the plasma bulk. The sheath electrons, for which the quasi-static approximation (QSA) nearly breaks down, are thus the best candidates for self-injection.

Meanwhile, the majority of electrons in the system (scattered black and bulk green in figure 6(a)) obey the quasi-static restrictions exceptionally well. The laser pulse and bubble overtake them over a time interval approximately equal to the bubble duration ($\sim 270\,\mathrm{fs}$ in this example). The striking similarity between the quasi-static electron density and the number density of non-quasi-static test electrons in figure 6(c) shows that the bubble on the whole is indeed a quasi-static structure, which enables precise WAKE modelling. The basic premise of the QSA is the absence of near-luminous particles travelling with the structure [29]. It was noticed many times that the faster the structure moves, the harder it is to violate the QSA and have injection [7, 47] (in our case, the bubble propagates with roughly a laser group velocity which gives $\gamma_\mathrm{g} \approx 63$). However, once the QSA restrictions are removed (which is the case of WAKE test particles) the injected electrons do show up. Indeed, figure 6(c) shows a dense bunch of test electrons near the base of the bubble, and figure 6(d) proves that these electrons were collected from the region of impact parameters of sheath electrons.

What made these test electrons enter the bubble? What physical phenomenon broke the quasi-static flow of electrons around the bubble?
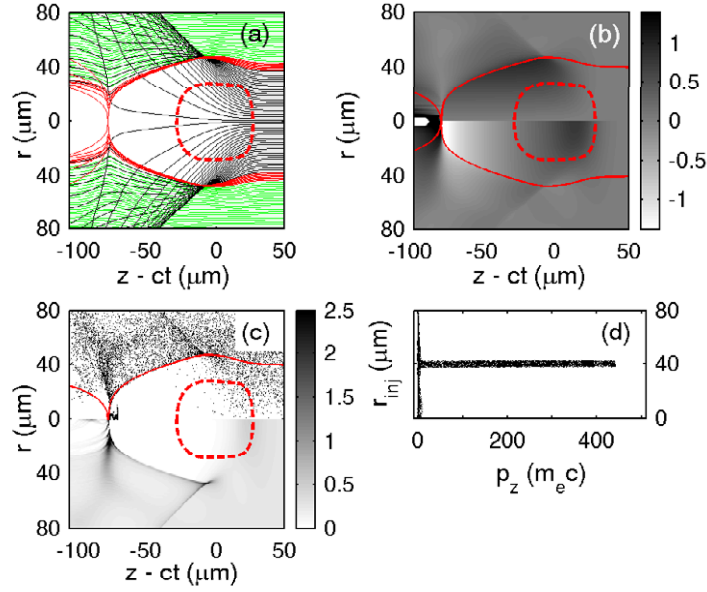
Figure 6. Electron bubble after the first nonlinear laser focus (position 1 in figure 8). Dashed red contour in panels (a)–(c) is the iso-contour of laser intensity at $\exp(-2)$ of the peak. (a) Trajectories $r_i(\xi)$ of the quasi-static WAKE macroparticles. (b) Time-averaged focusing $E_r - B_\theta$ (top half) and accelerating E_z (bottom half) fields acting on relativistic electrons. Fields are in units of $\mathrm{GV\,cm^{-1}}$. Thin red curves in (b) and (c) show trajectories of the innermost quasi-static WAKE macroparticles from the bubble sheath. (c) Top half shows positions of non-quasi-static test electrons (ξ_i, r_i), where $\xi = z - ct$. Each dot corresponds to one test particle. The number density of dots can be directly compared with the quasi-static electron density (in units of $10^{18}\,\mathrm{cm}^{-3}$) in the bottom half. (d) Initial radial positions of test electrons from the panel (c) versus their longitudinal momenta.

The answer can be derived from the fact that the laser-driven bubble is not a perfectly frozen, fully quasi-static one (i.e. depending only on variables r and $z - ct$). The quasi-static flow in the sheath breaks down due to a steady variation of the bubble shape caused by the nonlinear evolution of the driving pulse [14, 32, 48, 49]. (The other way to self-inject is to perturb the sheath instantly, by introducing a sharp downward density transition in the path of the bubble [50], or by the head-on collision of the driving laser with a very weak injection pulse [51, 52].)

The injection scenario in the longitudinally uniform plasma of low density ($\omega_0/\omega_{\mathrm{pe}} \sim 100$) is akin to trapping a relativistic projectile into the temporally expanding 3D potential bucket. As the laser pulse defocuses after the nonlinear focus, the bubble expands; if the expansion is rapid enough [14], some of the heavy sheath electrons lag behind the moving bubble boundary and stay inside the bubble. A large fraction of these electrons becomes trapped: their moving-frame (MF) Hamiltonian changes from $H_{\mathrm{MF}} = m_e c^2$ before the arrival of the pulse to $H_{\mathrm{MF}} < 0$, which would be impossible were the laser and bubble non-evolving [14] (note that QSA implies the conservation of H_{MF} [29]; thus, WAKE macroparticles cannot be trapped). If the bubble expands
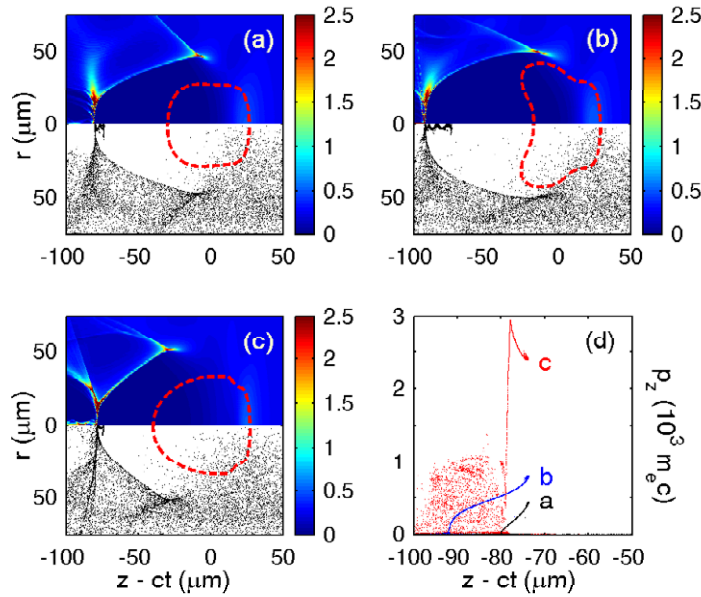
Figure 7. Electron injection in the expanding bubble. Electron density, in units of $10^{18}\,cm^{-3}$ (colour map), and test electrons (dots) are shown at (a) $z = 1.24\,cm$, (b) $z = 1.43\,cm$ and (c) $z = 2.2\,cm$ (positions 1–3 in figure 8). (d) Longitudinal momentum of electrons for (a)–(c) (labelled accordingly). Bubble expansion leads to self-injection with continuous momentum distribution. Shrinkage extinguishes the injection, shortens the bunch (electrons partly de-phase) and results in the phase space rotation.

and shrinks periodically (e.g. because of the spot size oscillations of the self-guided laser), self-injection may resume periodically [32]. Once the structure stabilizes, injection ceases.

4.2. Self-injection of test electrons in the evolving quasi-static plasma bubble

The evolution of the electron bubble and the dynamics of electron self-injection are shown in figure 7. Oscillations of the laser peak intensity and bubble size, and the locations where the injection occurs due to these oscillations are displayed in figure 8.

Figures 7(a)–(c) show the bubble at different positions within a centimetre distance after the first nonlinear focus (positions 1–3 in figure 8). The laser pulse tail confined in the bubble experiences periodic beatings, which cause alternating expansion and shrinkage of the accelerating bucket. The effect is further quantified in figure 8(b), where bubble length (distance from the first potential maximum to the first minimum on the axis) is plotted as a function of propagation distance. Bubble size is minimal slightly before the nonlinear focus ($z \approx 1\,cm$) and is largest at $z = 1.43\,cm$ (figure 7(b)). Figure 8(b) shows 12.5% expansion over the propagation distance 0.5 cm ($\sim$60 bubble lengths). Injection of initially quiescent ($\gamma_e = 1$) non-quasi-static test electrons goes uninterrupted during this stage, and, as is clear from figure 7(d), the electron energy/momentum spectrum is continuous. Contraction of the bubble between $z = 1.43$ and 2.2 cm (panels (b) and (c) of figure 7) extinguishes the injection and truncates the bunch. Particles remaining in the bucket are further accelerated. Electrons that were injected later are
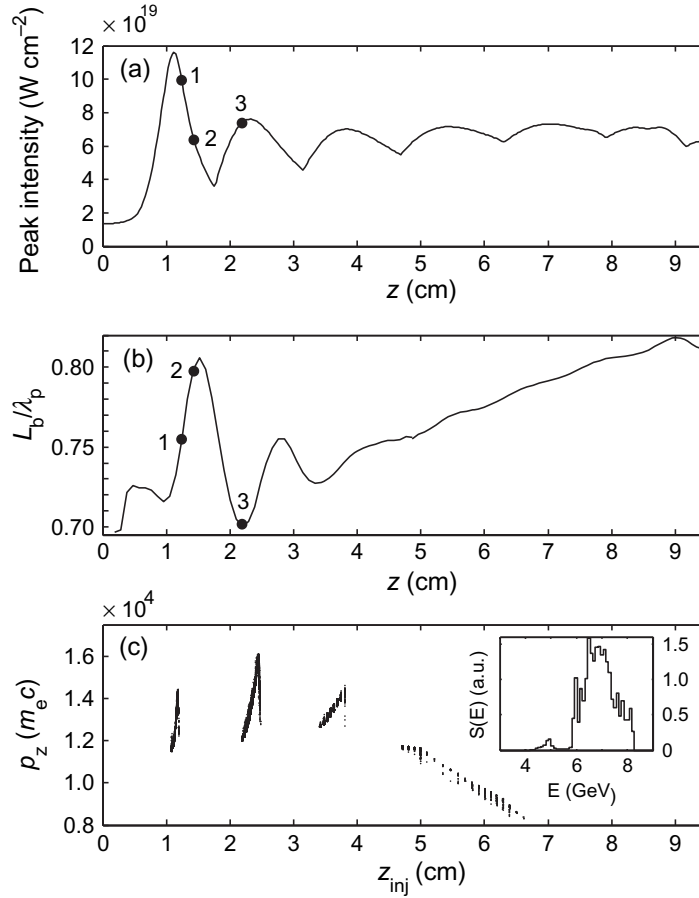
Figure 8. Periodic self-injection of test electrons in a homogeneous plasma (simulation of figure 7). (a) Peak intensity of the laser pulse. (b) Bubble length normalized to the linear wake period $\lambda_p = 2\pi c/\omega_{pe}$. Positions labelled 1–3 correspond to panels (a)–(c) of figure 7. (c) Longitudinal momentum of test electrons at the exit plane ($z = 10$ cm) versus the injection position; the inset shows the electron energy spectrum (number of electrons per spectrometer energy bin). The initially mismatched laser experiences periodic focusing and de-focusing (panel (a)). Self-injection of electrons occurs during the intervals of bubble expansion, which are closely correlated with the intervals of laser de-focusing. When the laser is self-guided, and the bubble changes steadily ($z > 4$ cm), self-injection is inefficient.

situated closer to the base of the bubble and are thus exposed to a higher accelerating force. The non-uniform accelerating gradient rotates the bunch phase space: soon after the injection ceases, the tail of the bunch catches up in energy with the head, and the energy spread decreases. Further evolution results in broadening of the electron spectrum (see, e.g., the phase space snapshot (c) in figure 7(d)). This kind of phase space rotation is different from that discussed in the literature [53]. As we shall see in section 4.3, this mechanism offers an opportunity for controllable generation of quasi-monoenergetic bunches well before the dephasing limit L_{deph} is reached.

Figure 8(a) shows that the peak laser intensity oscillates during the self-guiding stage. The bubble expands during the intervals of de-focusing (intensity reduction), and the self-injection resumes periodically. This is clearly seen from the particle tracking results in figure 8(c): the majority of accelerated electrons originate from the intervals of laser de-focusing located near $z \approx 1.1$, 2.4 and 3.75 cm. After $z = 4$ cm, the bubble grows very slowly and self-injection becomes inefficient. Finally, the three electron bunches merge in energy near the plasma exit, $z \approx 10$ cm. As a result, the energy spread, as shown in the inset in figure 8(c), appears to be rather large. A similar phenomenon of periodic injection and the resulting spectral broadening of the electron beam in centimetre-long gas-jet plasmas has been recently observed in the experiment [54].

Finally, test-particle modelling of electron acceleration in a uniform plasma of density $n_0 = 2.5 \times 10^{17}$ cm^{-3} predicts 7 ± 1 GeV energy gain over a 10 cm distance (as shown in the inset of figure 8(c)). Normalized transverse emittance of the bunch (i.e. the approximate area in phase space $\mathbf{r}_\perp \mathbf{p}_\perp$) is $\varepsilon_{N,\perp} = (m_e c)^{-1} (\langle r_\perp^2 \rangle \langle p_\perp^2 \rangle - \langle \mathbf{r}_\perp \mathbf{p}_\perp \rangle^2)^{1/2} \approx 7\pi$ mm mrad. Focusing field of the bubble is linear in radius in any transverse cross section (as seen in figure 6(b)). Therefore, as soon as the laser evolution stabilizes and self-injection terminates around $z \approx 4$ cm (i.e. the phase space of the bunch is filled), $\varepsilon_{N,\perp}$ is conserved [55].

Multiple electron injection deteriorates the electron energy spectrum and can also lead to emittance dilution. Electrons injected after $z = 2$ cm can be thus considered as unwanted 'dark current' [55]. To get rid of undesirable periodic injection, we need to reduce the nonlinear pulse evolution by using low-density plasmas, such as $n_0 \approx 10^{17}$ cm^{-3}. In this case, the pulse is initially matched for self-guiding, and, as figure 3 indicates, evolves very slowly. In a longitudinally homogeneous plasma of this low-density, blowout is not achieved even in the region of strongest focus; therefore, blowout and self-injection have to be enforced artificially.

To this end, we propose to overfocus the laser by a factor of $\sim$10 in intensity with a thin nonlinear plasma lens [33]. A short dense plasma slab shown in the inset of figure 9(a) (4 mm flat top with 1 mm linear ramps on either side), is placed immediately at the entrance and is followed by a long rarefied plasma in which blowout, self-injection and acceleration occur. Technically, the dense slab may be an embedded gas jet or a separate compartment of a differentially pumped cell. The density of the slab, $n_{sl} = 5 \times 10^{17}$ cm^{-3}, corresponds to $P/P_{cr} \approx 40$ and $\omega_{pe} \tau_L \approx 6$. Hence, the weakly focused laser beam released from the slab has a converging wave front imparted by the relativistic nonlinearity. Figure 9(a) shows that the focal length of the resulting thin lens is rather short: the peak laser intensity is achieved at 2.5 mm after the edge of the slab. The position of the nonlinear focal plane shifts insignificantly if the plasma after the slab is replaced with vacuum. The plasma lens is not free of aberrations. As a consequence, the nonlinear focal spot is not too small ($\approx$25 μm), and about 40% of pulse energy diffracts out of the box (instead of 5% in the uniform plasma case). After defocusing, the laser pulse is self-guided over 10 cm. This is the best case scenario for the LWFA because the blowout and electron injection occur only once (in the vicinity of the nonlinear focus) and then the wake remains mildly nonlinear and non-broken over the entire propagation distance (the same as studied in [6, 9, 10]). Figures 9(b) and (c) show once more that self-injection occurs during the laser de-focusing and bubble expansion. Subsequent bubble shrinkage stops self-injection and shortens the bunch. Electrons remaining in the first bucket are further accelerated to 2.5 GeV energy with a 2.35% spread (inset of figure 9(c)).
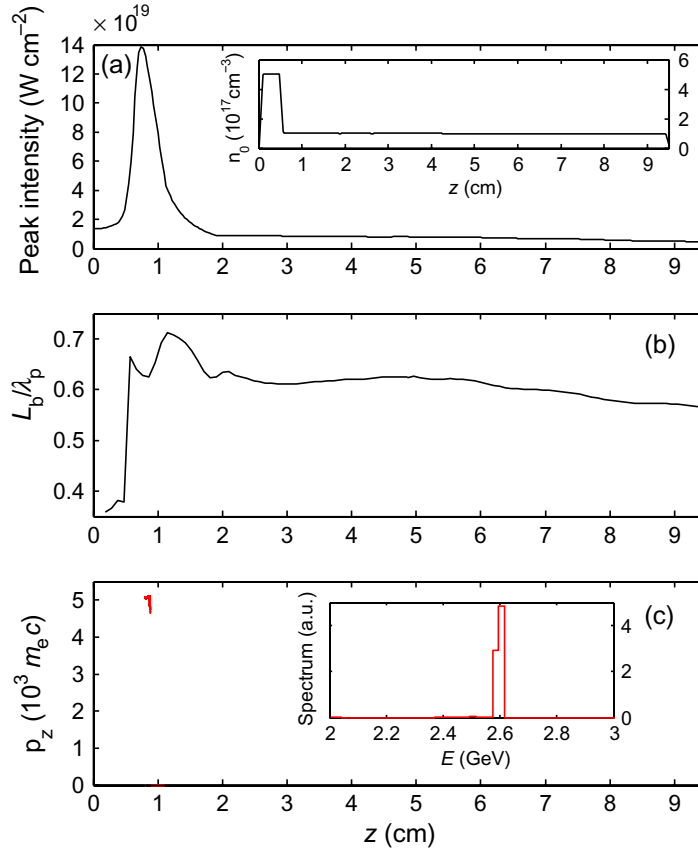
Figure 9. Test electron injection enforced by the laser pre-focusing with a plasma lens. (a) Peak intensity of the laser pulse. Inset: longitudinal profile of electron density. (b) Normalized length of the first wake bucket. (c) Longitudinal momentum of test electrons from the first bucket at the exit plane ($z = 10$ cm); inset: the electron energy spectrum. The laser pulse released from the dense slab is focused on the rarefied plasma and locally produces electron blowout. Electrons are self-injected during the laser de-focusing and bubble expansion. Subsequent contraction of the first bucket stops injection. The laser becomes self-guided and the plasma wake remains weakly nonlinear after $z \approx 1.8$ cm; as seen in (c), self-injection never resumes. This helps reduce the electron energy spread to 2%.

4.3. Dynamics of electron self-injection in the quasi-cylindrical 3D PIC simulations

We complement the test-particle study of the electron injection and acceleration with the fully dynamic simulations (with beam loading included) using the recently developed quasi-cylindrical 3D PIC code CALDER-Circ [31]. This code is highly efficient for the treatment of quasi-paraxial laser propagation in rarefied plasmas because it (i) preserves the realistic geometry of interaction and (ii) accounts for the axial asymmetry by decomposing the electromagnetic fields (laser and wake) into a few azimuthal modes. Thus, the 3D problem is reduced to an essentially 2D one. Reduced simulation load due to the favourable simulation geometry (well-preserved axial symmetry) and reduced description of the radiation beam makes it possible to accomplish the quasi-cylindrical PIC modelling within time scales unaccessible
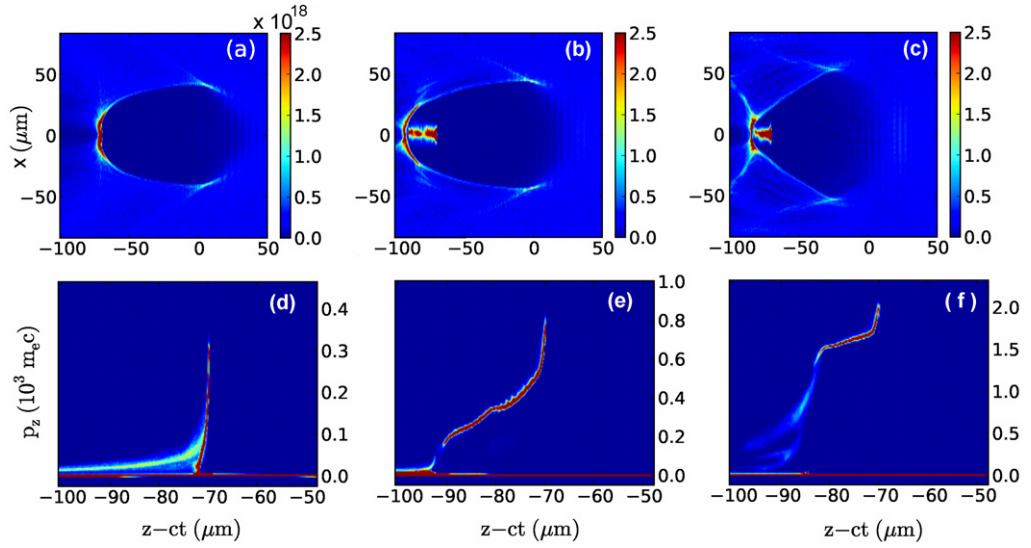
Figure 10. Electron injection during a bubble oscillation period in the quasi-cylindrical CALDER-Circ simulation. Background density $n_0 = 2.5 \times 10^{17}$ cm^{-3}. The top row shows electron density in units of cm^{-3} (in the plane $y = 0$ orthogonal to the laser polarization). The bottom row depicts the corresponding longitudinal momentum distribution. Panels (a) and (d) correspond to the propagation distance $z = 0.14$ cm; (b) and (e) $z = 0.336$ cm; (c) and (f) $z = 1.04$ cm. Panels (a)–(c) are direct counterparts of panels (a)–(c) of figure 7.

for full 3D PIC codes. Details of the numerical realization and the required computing resources are given in the appendix and in [31].

The aim of our CALDER-Circ modelling is twofold. Firstly, as a part of code benchmarking, we validate the dynamical behaviour of the laser and the bubble observed earlier in the quasi-paraxial, quasi-static WAKE modelling (e.g. features demonstrated in figure 7). Secondly, electron injection and acceleration during the period of bubble expansion and shrinkage (predicted in test-particle modelling with a quasi-statically evolving bubble) are reproduced in the fully dynamic mode, and with beam loading accounted for; this allows for meaningful predictions of the experimental outcome.

To explore the dynamics of electron injection, we skip the most time-consuming part of the laser self-focusing from the 80 μm spot to the minimal spot size ∼25 μm, and start all the runs with a Gaussian, linearly polarized (in the y-direction) laser focused at the plasma edge to a spot of $r_0 = 27.4$ μm (which corresponds exactly to figure 2(b)). The peak intensity 1.15×10^{20} W cm^{-2} is the same as in figure 2(b). The plasma density profile is flat-top with a 0.3 mm linear front ramp. We report here results of two 1.5-cm-long runs for plasma densities $n_0 = 2.5 \times 10^{17}$ (figures 10 and 11) and 10^{17} cm^{-3} (figure 12).

The reason why we can ignore the evolution of the laser before the nonlinear focus, and thus significantly reduce the simulation load, can be derived from WAKE simulations of section 3.2. Firstly, the pulse envelope in the nonlinear focus usually shows no signatures of beam break-up, which enables a Gaussian fit. This is true for the entire density range 1–2.5 × 10^{17} cm^{-3}. Secondly, comparison of red and blue curves in figure 2(a) shows that once the pulse is tightly focused, defocusing continues in nearly the same fashion no matter whether the pulse was
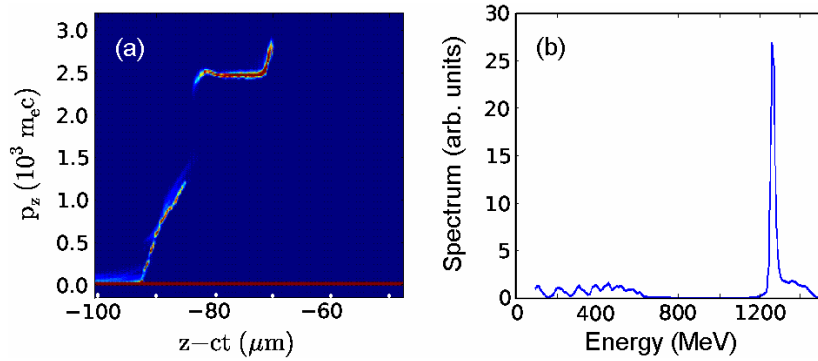
Figure 11. Electron energy after 1.5 cm propagation in the simulation of figure 10. (a) Longitudinal momentum distribution in arbitrary units; (b) electron energy spectrum. Phase space rotation has generated a monoenergetic electron bunch ($\Delta E/E \approx 2.3\%$) centred at 1.25 GeV. The charge in the monoenergetic bunch is 1.3 nC.

perfectly Gaussian or had previously passed through a rather rough nonlinear focusing (in other words, nonlinear focusing does not incur significant aberrations). Finally, once the plasma density and laser power are fixed, average spot size and intensity of the self-guided pulse are insensitive to the initial spot size.

The top row of figure 10 displays the bubble (laser field not shown) at the positions where (a) the electron injection begins ($z = 0.14$ cm); (b) the bubble is the largest, and the electron beam is the longest ($z = 0.336$ cm); (c) the bubble is the shortest, and the electron bunch is truncated by $\sim 40\%$ due to the contraction of the accelerating bucket ($z = 1.04$ cm). These plots are the closest counterparts of figures 7(a)–(c) (which correspond to the distances $z - z_{\text{foc}} = 0.14, 0.33$ and 1.1 cm from the nonlinear focus). There is a striking similarity between the bubble dynamics in WAKE (cylindrically symmetric, quasi-paraxial and time-averaged) and that in the CALDER-Circ runs, except that the bubble contraction is less dramatic in the full PIC run (transverse self-fields of the electron bunch resist the contraction [42]). We should emphasize that the beam loading alone is unable to extinguish self-injection. To evaluate its contribution, we approximate the electron bunch from figure 10(c) with a flat-top distribution with a Gaussian radial profile, $n_b(r) = n_{b0} \exp(-r^2/\sigma_b^2)$, where $n_{b0} = (Q_b/|e|)(\pi \sigma_b^2 l_b)^{-1} \approx 7 \times 10^{18} \text{ cm}^{-3}$ is the peak electron density, $Q_b \approx 1.3$ nC is the total charge, $\sigma_e \approx 5 \, \mu$m is the root mean square (rms) spot size and $l_b \approx 15 \, \mu$m is the length of the bunch. According to Tzoufras et al [42], the sheath electrons cross the axis, and the bubble remains closed until $R_b^4/(8r_t^2 \Lambda_0) > 1$, where $\Lambda_0 = \int_0^\infty r \, (n_b/n_0) \, dr = (\sigma_e^2/2)(n_{b0}/n_0)$ is the normalized charge per unit length, r_t is the bubble radius in the transverse cross-section taken at the front tip of the bunch and R_b is the bubble radius in the central cross-section. Figure 10(c) gives $\Lambda_0 \approx 350 \, \mu\text{m}^2$, $r_t \approx 23 \, \mu$m and $R_b \approx 53 \, \mu$m. Hence, $R_b^4/(8r_t^2 \Lambda_0) \approx 5.3$ and the bubble is not fully loaded. Moreover, CALDER-Circ simulation clearly indicates that injection continues uninterrupted until the moment of bubble stabilization, and gets extinguished by the subsequent contraction. Transverse fields of the bunch are unable to preclude the bucket contraction; the bubble dynamics and the process of electron self-injection are thus governed primarily by the evolution of the driver rather than by collective fields of trapped electrons.
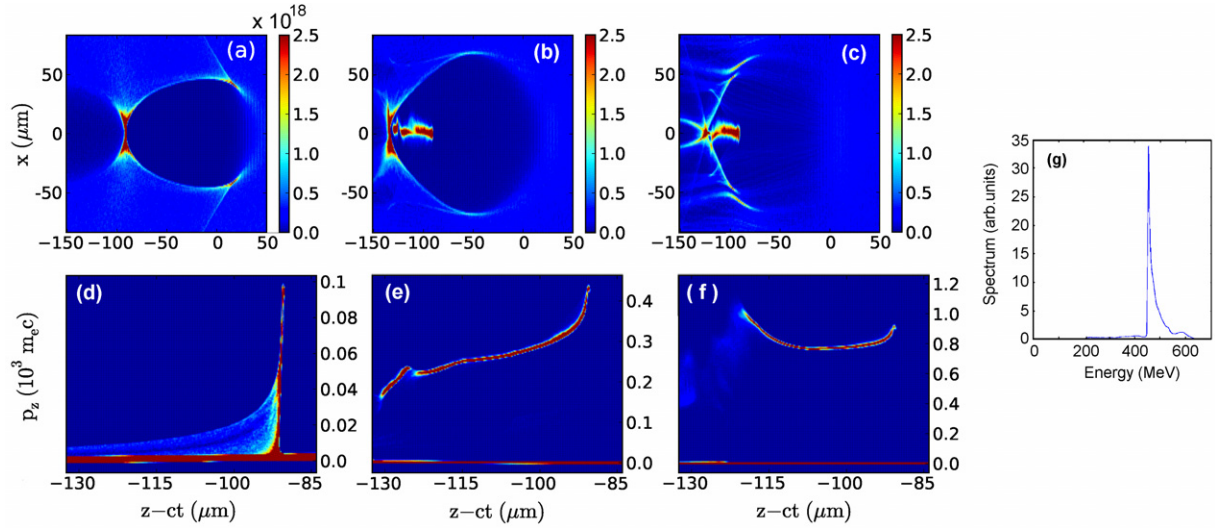
Figure 12. Electron injection during bubble expansion in the quasi-cylindrical CALDER-Circ simulation. Background density is $n_0 = 10^{17}\,\text{cm}^{-3}$. Quantities are the same as in figure 10. Panels (a) and (d) correspond to the propagation distance $z = 0.83\,\text{mm}$; at this moment, the injection features become clear. Panels (b) and (e) correspond to $z = 0.47\,\text{cm}$; here, the bubble is the largest, and injection ceases. Panels (c), (f) and (g) correspond to $z = 1.5\,\text{cm}$, where the phase space rotation creates a monoenergetic bunch.

The effect of beam loading, however, effectively reduces the accelerating gradient and makes its longitudinal variation along the bunch less steep [42]. As a result, the electron phase space displayed in the bottom row of figure 10 bears only a limited similarity to the results of test-electron modelling presented in figure 7(d). Electrons in the front tip of the bunch are accelerated to the same energy as test electrons, whereas the bunch body experiences a lower (and more longitudinally homogeneous) accelerating gradient. However, the resulting slow down of phase space rotation does not preclude formation of the monoenergetic electron beam (see figure 11).

Before the end of the simulation, the bubble starts expanding again. Figure 11 shows the second group of injected electrons. This phenomenon of periodic injection is familiar from the previous subsection. Yet at $z = 1.5\,\text{cm}$ these non-monoenergetic electrons are well separated from the leading bunch, which has the central energy 1.25 GeV, 2.3% RMS energy spread and 1.3 nC charge. The 45 fs bunch duration extracted from figure 11(a) gives the average current of 30 kA. Assuming that the accelerating gradient is preserved over the rest of LPI distance (7 cm), the final energy gain can be estimated as 7 GeV, which is within the interval given by the test particle modelling (inset of figure 8(c)). At $z = 1.5\,\text{cm}$, the RMS spot size of the bunch is 5 μm, and the angular divergence is 6 mrad. Normalized transverse emittances, $\varepsilon_{N,i} = (m_e c)^{-1} (\langle x_i^2 \rangle \langle p_i^2 \rangle + \langle x_i p_i \rangle^2)^{1/2}$, are $\varepsilon_{N,x} = 11.3\pi$ mm mrad and $\varepsilon_{N,y} = 12.1\pi$ mm mrad. As the focusing field is linear in x and y, and the bubble evolves slowly, $\varepsilon_{N,i}$ are adiabatic invariants, and are thus expected to be measured in the experiment.

Secondary injection in the same bucket, which is clearly seen in figure 11(a), can eventually contaminate the monochromatic energy spectrum and cause emittance dilution. Therefore,

having simulated only the initial stage, we cannot predict exactly the amount of dark current and final energy spread and emittance. On the other hand, simulation in the same geometry with $n_0 = 10^{17}\,cm^{-3}$ (shown in figure 12) is dark current free.

Bubble expansion appears to be significantly stronger than in the high-density case. Subsequent strong shrinkage (expected from the WAKE simulation of figure 9) is actually not observed. This is mainly because the large injected charge (~ 1.5 nC, similar to the higher-density run) results in considerable beam loading. However, the bunch parameters extracted from the simulation at the instant corresponding to figure 12(b) give $R_b^4/(8r_t^2 \Lambda_0) \approx$ 2.5, and the beam loading is again unable to prevent contraction of the bucket. As a result the bunch tail is truncated, accelerated charge decreases to 1.3 nC, and injection terminates as soon as the bubble size stabilizes. With a 100 fs bunch duration inferred from figure 12(f), the average current is 13.5 kA. At the end of the simulation (figures 12(f) and (g)), the tail of the bunch catches up in energy with the head, and the single monoenergetic bunch is formed ($\Delta E/E \approx 1.5\%$) with the central energy $E = 460$ MeV. Extrapolation to further 7 cm acceleration distance gives 2.6 GeV, which is again close to the test-particle prediction. Normalized transverse emittances are roughly 40% lower than in the higher density case of figures 10 and 11. As seen in figure 12(e), the first wake bucket is no longer the evacuated bubble; hence, self-injection will not resume, and the low relative energy spread and emittance are likely to be preserved.

To conclude, the quasi-cylindrical 3D PIC simulations have reproduced in a fully dynamical mode (with the beam loading effect included) all the basic features of the plasma bubble evolution discovered in the quasi-static WAKE modelling: electron self-injection during bubble expansion, termination of injection and formation of the monoenergetic bunch during bubble stabilization and contraction.

5. Conclusion

The new short-pulse (100–200 fs) generation of PW laser facilities [3, 4] opens the path towards single-stage multi-GeV laser wakefield accelerators. The reported comprehensive numerical study of the regimes accessible to such lasers clearly shows robustness of laser pulse self-guiding and self-injection and acceleration of background plasma electrons in the blowout regime. It is found that at low plasma density (which is mandatory for the PW laser stability) electron self-injection critically depends on the nonlinear evolution (i.e. RSF and refraction) of the driving pulse. Manipulation with the PW pulse dynamics using the nonlinear focusing properties of plasmas (e.g. by tailoring the background plasma density in a specially designed target, such as multi-sectioned differentially pumped cell), helps achieve a high degree of control over electron self-injection and, hence, adjust the quality of accelerated bunch. The basic features of the envisioned laser wakefield experiment (with laser parameters corresponding to the TPW facility) can be summarized as follows.

- The 1.33 PW, 150 fs pulse is self-guided over 10 cm in uniform plasmas of density $1–3 \times 10^{17}\,cm^{-3}$.
- Although self-guiding appears to be quite insensitive to the imperfection of laser beam focusing, high quality of the focal spot is essential for quasi-monoenergetic electron acceleration.

IOP Institute of Physics ⬥ DEUTSCHE PHYSIKALISCHE GESELLSCHAFT

- Electrons are self-injected into the plasma wake. Electron blowout and self-injection are enforced by nonlinear focusing of the laser beam inside the plasma.
- An electron bunch containing about 1.3 nC charge is accelerated to 2.5–7 GeV energy with less than 10% energy spread and a normalized transverse emittance of $5–10\pi$ mm mrad.

Predicted single shot average beam currents in the range 10–30 kA, together with multi-GeV electron energy and a few per cent relative energy spread, make the PW laser-driven wakefield accelerator a very promising candidate for such demanding applications as compact and brilliant ultrashort pulse synchrotron sources [56]–[58].

Appendix. High-performance computing resources for cylindrical PIC simulations

The quasi-cylindrical PIC code used for the simulations in section 4.3 was developed on the basis of the fully electromagnetic 3D PIC code CALDER [59]. The code is fully parallelized with the message-passing interface. The simulation box is divided into smaller boxes along the longitudinal direction and a core is assigned to each of them. The code runs on the 'Titane' cluster at the CEA facility of Bruyères-Le-Châtel. It is made of 1092 Bull Novascale R422 servers. Each server is composed of two Intel Xeon 5570 quad-core processors running at 2.93 GHz and they have 24Go of memory (3Go core $^{-1}$). The purpose of parallelization is to accelerate the run and gather sufficient memory to be able to simulate the required number of particles. The performance scales linearly with the number of cores up to a threshold depending on the grid size. We use 250 cores, which is below the linear scaling threshold in our case. The fields are approximated in 3D through decomposition on two poloidal modes, whereas the particles are in full 3D. Each 2D grid cell is seen by the particles as a torus in space (formed by the revolution of the grid cell around the propagation axis) and, as a consequence, we need to take a large number of particles per cell with respect to what 2D PIC codes usually require. In the runs presented in this paper, we have 15 particles per cell, which provides enough accuracy to see both the injection and beam loading effects. In [31], it is shown that in the case of a linearly polarized laser, modes of order $m \geqslant 2$ contribute weakly to the electric field. Our restriction to modes $m = 0$ and $m = 1$ is therefore a very good approximation that allows us to simulate the propagation up to 1.5 cm in 21 500 CPU hours (86 h on 250 cores) for the higher-density case and 32 500 CPU hours (130 h on 250 cores) for the low-density case. In both runs, resolution in the direction of propagation is $\Delta z = 0.125 c/\omega_0$, and $\Delta r = 0.4\lambda_0$ is the radial grid size. The time step is $\Delta t = 0.124\omega_0^{-1}$. The number of grid points

is $10\,000(\text{in } z) \times 600(\text{in } r) = 6 \times 10^6$ for the higher density, and $12\,000 \times 800 = 9.6 \times 10^6$ for the low-density case (where a larger box size was dictated by a larger spot of the diffracted laser).

References

[1] Aoyama M, Yamakawa K, Akahane Y, Ma J, Inoue N, Ueda H and Kiriyama H 2003 *Opt. Lett.* **28** 1594
[2] Hooker C J *et al* 2006 *J. Phys. IV France* **133** 673
[3] Martinez M *et al* 2006 *Proc. SPIE* **5991** 59911N
[4] Hein J, Kaluza M C, Bödefeld R, Siebold M, Podleska S and Sauerbrey R 2006 *Lect. Notes Phys.* **694** 47 (see also http://www.physik.uni-jena.de/inst/polaris/)
[5] Khazanov E A and Sergeev A M 2008 *Phys.—Usp.* **51** 969
[6] Gorbunov L M, Kalmykov S Y and Mora P 2005 *Phys. Plasmas* **12** 033101
[7] Lu W, Tzoufras M, Joshi C, Tsung F S, Mori W B, Vieira J, Fonseca R A and Silva L O 2007 *Phys. Rev. ST Accel. Beams* **10** 061301
[8] Tajima T and Dawson J M 1979 *Phys. Rev. Lett.* **43** 267
[9] Lifschitz A F, Faure J, Glinec Y, Malka V and Mora P 2006 *Laser Part. Beams* **24** 255
[10] Kalmykov S Y, Gorbunov L M, Mora P and Shvets G 2006 *Phys. Plasmas* **13** 113102
[11] Rosenzweig J B, Breizman B N, Katsouleas T and Su J J 1991 *Phys. Rev.* A **44** R6189
[12] Pukhov A and Meyer-ter-Vehn J 2002 *Appl. Phys.* B **74** 355
[13] Gordienko S and Pukhov A 2005 *Phys. Plasmas* **12** 043109
[14] Kalmykov S, Yi S A, Khudik V and Shvets G 2009 *Phys. Rev. Lett.* **103** 135004
[15] Leemans W P, Nagler B, Gonsalves A J, Tóth C S, Nakamura K, Geddes C G R, Esarey E, Schroeder C B and Hooker S M 2006 *Nat. Phys.* **2** 696
[16] Karsch S *et al* 2007 *New J. Phys.* **9** 415
[17] Hafz N A M *et al* 2008 *Nat. Photon.* **2** 571
[18] Osterhoff J *et al* 2008 *Phys. Rev. Lett.* **101** 085002
[19] Kneip S *et al* 2009 *Phys. Rev. Lett.* **103** 035002
[20] Froula D *et al* 2009 *Phys. Rev. Lett.* **103** 215006
[21] Ross I N, Collier J L, Matousek P, Danson C N, Neely D, Allott R M, Pepler D A, Hernandez-Gomez C and Osvay K 2000 *Appl. Opt.* **39** 2422
[22] Esarey E, Schroeder C B and Leemans W P 2009 *Rev. Mod. Phys.* **81** 1129
[23] Sun G Z, Ott E, Lee Y C and Guzdar P 1987 *Phys. Fluids* **30** 526
[24] Andreev N E, Gorbunov L M, Mora P and Ramazashvili R R 2007 *Phys. Plasmas* **14** 083104
[25] Sprangle P, Esarey E and Ting A 1990 *Phys. Rev.* A **41** 4463
[26] Decker C D, Mori W B, Tzeng K C and Katsouleas T 1996 *Phys. Plasmas* **3** 2047
[27] Reed S A *et al* 2009 *AIP Conf. Proc.* **1086** 177
[28] Kalmykov S Y *et al* 2010 *High Energy Density Phys.* at press doi:10.1016/j.hedp.2009.11.002
[29] Mora P and Antonsen T M Jr 1997 *Phys. Plasmas* **4** 217
[30] Pukhov A 1999 *J. Plasma Phys.* **61** 425
[31] Lifschitz A F, Davoine X, Lefebvre E, Faure J, Rechatin C and Malka V 2009 *J. Comput. Phys.* **228** 1803
[32] Oguchi A, Zhidkov A, Takano K, Hotta E, Nemoto K and Nakajima K 2008 *Phys. Plasmas* **15** 043102
[33] Ren C, Duda B J, Hemker R G, Mori W B, Katsouleas T, Antonsen T M Jr and Mora P 2001 *Phys. Rev.* E **63** 026411
[34] Perelomov A M, Popov V S and Terentev M V 1965 *Sov. Phys.—JETP* **23** 924
[35] Ammosov M V, Delone N B and Kraünov V P 1986 *Sov. Phys.—JETP* **64** 1191
[36] Matlis N H *et al* 2006 *Nat. Phys.* **2** 749
[37] Dong P *et al* 2010 *New J. Phys.* **12** 045016
[38] Thomas A G R *et al* 2007 *Phys. Rev. Lett.* **98** 095004

[39] Faure J, Glinec Y, Santos J J, Ewald F, Rousseau J P, Kiselev S, Pukhov A, Hosokai T and Malka V 2005 *Phys. Rev. Lett.* **95** 205003

[40] Faure J, Glinec Y, Gallot G and Malka V 2006 *Phys. Plasmas* **13** 056706

[41] Ralph J E, Marsh K A, Pak A E, Lu W, Clayton C E, Fang F, Mori W B and Joshi C 2009 *Phys. Rev. Lett* **102** 175003

[42] Tzoufras M, Lu W, Tsung F S, Huang C, Mori W B, Katsouleas T, Vieira J, Fonseca R A and Silva L O 2009 *Phys. Plasmas* **16** 056705

[43] Rechatin C, Davoine X, Lifschitz A, Ben Ismail A, Lim J, Lefebvre E, Faure J and Malka V 2009 *Phys. Rev. Lett.* **103** 194804

[44] Esirkepov Zh T, Kato Y and Bulanov S V 2008 *Phys. Rev. Lett.* **101** 265001

[45] Lu W, Huang C, Zhou M, Tsoufras M, Tsung F S, Mori W B and Katsouleas T 2006 *Phys. Plasmas* **13** 056709

[46] Mora P 2009 *Eur. Phys. J. Spec. Top.* **175** 97

[47] Kostyukov I, Nerush E, Pukhov A and Seredov V 2009 *Phys. Rev. Lett.* **103** 175003

[48] Hemker R G, Hafz N M and Uesaka M 2002 *Phys. Rev. ST Accel. Beams* **5** 041301

[49] Xu H, Yu W, Lu P, Senecha V K, He F, Shen B, Qian L, Li R and Xu Z 2005 *Phys. Plasmas* **12** 013105

[50] Suk H, Barov N, Rosenzweig J B and Esarey E 2001 *Phys. Rev. Lett* **86** 1011

[51] Davoine X, Lefebvre E, Rechatin C, Faure F and Malka V 2009 *Phys. Rev. Lett.* **102** 065001

[52] Malka V, Faure J, Rechatin C, Ben-Ismail A, Lim J K, Davoine X and Lefebvre E 2009 *Phys. Plasmas* **16** 056703

[53] Tsung F S, Narang R, Mori W B, Joshi C, Fonseca R A and Silva L O 2004 *Phys. Rev. Lett.* **93** 185002

[54] Hafz N A M, Lee S K, Jeong T M and Lee J 2010 *Nucl. Instrum. Methods Phys. Res.* A at press doi:10.1016/j.nima.2010.02.020

[55] Rosenzweig J B 2003 *Fundamentals of Beam Physics* (New York: Oxford University Press) p 100

[56] Rousse A *et al* 2004 *Phys. Rev. Lett.* **93** 135005

[57] Grüner F *et al* 2007 *Appl. Phys.* B **86** 431

[58] Schlenvoight H P *et al* 2008 *Nat. Phys.* **4** 130

[59] Lefebvre E *et al* 2003 *Nucl. Fusion* **43** 629